Photoacoustic ToF Tomography of Blood Cells: From Mathematical Approximation to Super-resolution

Ayush Bhandari
Massachusetts Inst. of Tech.
Cambridge, 02139-4307 USA
ayush@MIT.edu

Eric M. Strohm
University of Toronto
Toronto, Ontario, M5G 1M1, Canada
eric.strohm@utoronto.ca

Michael C. Kolios
Ryerson University
Toronto, M5B 2K3 Canada
mkolios@ryerson.ca

Ramesh Raskar
Massachusetts Inst. of Tech.
Cambridge, 02139-4307 USA
raskar@MIT.edu

***Abstract*—Photoacoustic or PA waves, generated from blood cells, create distinct spectral features in the Fourier domain, for example, maxima and minima. In this way, high-frequency PA signals can be used to identify and distinguish blood cells. However, due to finite bandwidth of physical systems, many interesting Fourier features are invisible within the observed bandwidth. To overcome this challenge, we reformulate the PA imaging problem as a time-of-flight super-resolution problem. Based on the PA wave equations, we show that the problem reduces to estimation of sparse cellular features from a set of finite trigonometric moments. For this purpose, we develop a super-resolution algorithm which achieves near exact performance (in context of maximum likelihood estimation) when working with experimental data. Hence, our work alleviates an important bottleneck in PA imaging linked with classification of cellular features.**

I. Introduction

Mathematical imaging in life sciences is the key to understanding biological features ranging from molecular to anatomical scales. While ultrasound imaging, MRI and computed tomography are well established imaging methods at the anatomical level, a number of challenges still remain at the microscopic level. Some attributes include penetration depth, spatial-temporal resolution as well as imaging contrast.

To this end, photoacoustic or PA imaging proves to be advantageous in many ways [1]. As the name suggests, the PA effect is the conversion or transformation of electromagnetic energy into acoustic energy—a phenomenon that was first observed by Alexander Graham Bell in 1880 [2]. Qualitatively speaking, the interaction of an optical excitation pulse with a material results in a rise in temperature. Although infinitesimal ($\sim$ milli kelvin [3]), the rise in temperature is enough to catalyze thermoelastic expansion resulting in stress waves that manifest as acoustic energy. Due to the fact that PA imaging utilizes a combination of light and sound in the process of imaging, disadvantages in one regime (for example, sound) can be compensated by the other. A concrete example is that of biological tissues. Tissues are known to scatter light but this is orders of magnitude lesser in the case of sound. Therefore, PA imaging offers greater penetration depth [1].

Due to the numerous advantages centric to the PA imaging technology [3], [4], within the the last decade, there has been a surge of research interest in this area. This includes development of efficient instrumentation as well as mathematical algorithms for solving inverse problems. For a detailed overview of the topic, we refer to [5].

As pointed out in [6], the shape of the PA wave encodes important information linked with physical parameters such as dimensions, sound speed and density. By capitalizing on this aspect of PA imaging, recently, Strohm and Kolios [7] developed a label–free technique for classification of cell types: red blood cells (RBC), white blood cells (WBC) and circulating melanoma cells (CMC). This one of a kind imaging modality was the first demonstration of a setup capable of (a) identification of cells, as well as (b) estimation of the cell size. Thus leading to a classification algorithm that can distinguish cancer cells from their healthy counterparts, besides understanding cell morphology [8].

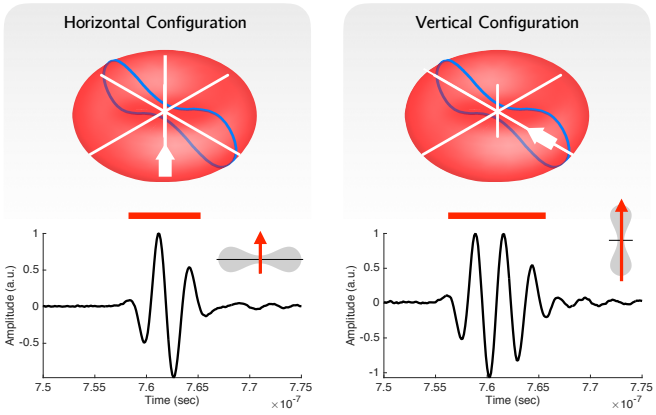

Fig. 1. Photoacoustic measurements of single RBC. The cross-section of the biconcave RBC is shown in blue ink. The arrow shows the direction of wave/pulse propagation. (a) Horizontal configuration with minimal spread in time-domain. (b) Vertical configuration with a larger spread in time-domain. The red bars mark the approximate time-spread of the pulses. Also see Fig. 4.

The approach discussed in [7] is based on the *spectral periodicity* of the measured data. By computing the power spectrum of the measurements, the authors argue that cell parameters are related to spectral features such as the inter-spacing between two consecutive minima. This heuristic approach works whenever the spectral features are distinctly visible. However, this may not always hold.

Let us begin with a discussion on the mathematical intuition behind the visibility of spectral features. Consider the case of RBCs which have a biconcave shape. This is shown in Fig. I (also check Fig. 4 for clarity) where we overlay the biconcave cross-section in blue ink and the approximate time spread (similar to full width at half maximum) in red ink. When a pulse or a wave propagates in the horizontal configuration (cf. Fig. 4, $\theta = 0$), it is reflected by the cell walls. The resulting PA pulse echo measurement has minimal spread in time-domain as the pulse propagates through the center of the RBC—the point of minimum thickness[1]. On the other hand, in the vertical configuration, the PA pulse echo measurement has a larger spread in time-domain as the pulse propagates through the diameter[2] of the cell.

As an example, assume that two dominant reflections of equal intensity occur in any possible configuration. Much in the same way as time-of-flight or ToF imaging [9], we may model the reflectors or sources as,

$$h(t) = \delta\left(t - \tfrac{d_1}{\nu}\right) + \delta\left(t - \tfrac{d_2}{\nu}\right)$$

where $d_k, k = 1, 2$ are the relative locations of the reflectors from the sensor, ν is the propagation speed and δ denotes the Dirac distribution.

[1]This corresponds to a physical distance of 0.8–1.0 μm.
[2]This corresponds to a physical distance of 6.2–8.2 μm.

978-1-5386-1565-2/17/$31.00

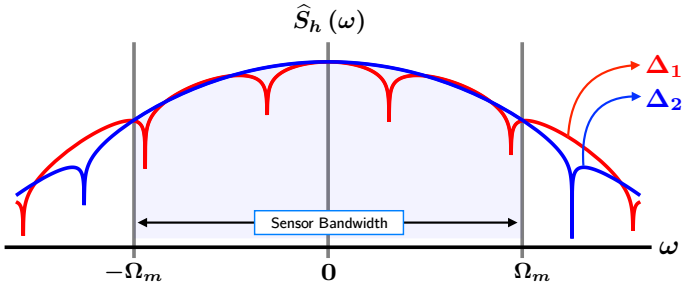

Fig. 2. Power spectrum of low-pass measurements: $\widehat{B}_h(\omega) = \widehat{S}_h(\omega)\, b(\omega)$ where $b(\omega)$ is the frequency response of the low-pass measurement device. With $\Delta_2 < \Delta_1$, no spectral minima occur in the bandwidth $\omega \in [-\Omega_m, \Omega_m]$.

Let $\Delta = |d_2 - d_1|$ be the separation between the cell walls and $\widehat{h}(\omega) = \int h(t)\, e^{-\jmath\omega t} dt$ denote the Fourier transform of h. Then, the power spectrum of h denoted by $\widehat{S}_h$ is $\widehat{S}_h(\omega) \triangleq |\widehat{h}(\omega)|^2 = 4\cos^2\left(\frac{\omega\Delta}{2\nu}\right)$.

Since most physical devices have a finite bandwidth, observations are written as $\widehat{B}_h(\omega) = \widehat{S}_h(\omega)\, b(\omega)$ with $b(\omega) = 0, |\omega| > \Omega_m$. As the inter-spacing Δ between the cell walls decreases, it is very likely that none of the spectral minima are visible within the bandwidth. This is shown in Fig. 2 where $\Delta_2 < \Delta_1$ and $b(\omega)$ is chosen to be a Gaussian window. This approach is similar to cepstral analysis used in acoustic microscopy (cf. pg. 157, [10]). Clinical and pre-clinical systems typically have a bandwidth $\Omega_m < 60$ MHz and lack the sensitivity to detect signals from single cells. UHF transducers used for single cell imaging have 200–500 MHz bandwidth [7], [11]. However, observing all cellular features ranging 5–30 μm requires bandwidths in the GHz range [11]. Our simple mathematical reasoning justifies the bottleneck quoted in [7] (cf. pg. 744):

> It was not possible to calculate the RBC size, as the spectral fitting method is highly sensitive to the orientation of the RBC relative to the transducer, and the orientation could not be determined in these measurements.

Can we do better than this? Overcoming this computational drawback has important consequences in (a) cell counting and classification [7] specially in the context of circulating tumor cells and cancer related diagnosis, and (b) understanding cell morphology [8]. The main goal of this paper is to formalize the inverse problem of accurate estimation of cell parameters from the PA measurements which allows us to recover cell parameters (not limited to RBCs) from PA measurements. Starting with the wave equations of PA imaging, we reformulate the inverse problem as a time-of-flight or ToF estimation problem [9], [12] whereby estimating cell parameters amounts to temporal super-resolution given a finite set of trigonometric moments.

A. Organization of this paper

In Section II, we develop the PA wave equation solution for cellular ToF imaging problem. We discuss the solution to the inverse problem of ToF estimation in Section III. In Section IV, we validate our approach with PA measurements based on RBCs and CMCs. Finally we conclude in Section V.

II. Problem Setup: Photoacoustic ToF Imaging

A. ToF Imaging Pipeline

The main components of any ToF imaging [9] modality are the probing function, $p(t)$, the scene response function (SRF), $h(t,\tau)$ and the instrument response function (IRF), $\varphi(\tau, t)$.

Said simply, the probing function "probes" the scene. This may be a pulse or a continuous wave function, such as a sinusoid [13]. The interaction between the probing function and the SRF results in the reflected signal (equivalent to PA wave generated signal in PA imaging),

$$r(t) = \int p(\tau)\, h(t,\tau)\, d\tau. \tag{1}$$

For example, in ranging or time-delay estimation problems, $h(t,\tau) = \Gamma_0 \delta(t - \tau - t_0)$ where Γ_0 is the intensity of an object at a distance d_0 which results in delay $t_0 = 2d_0/\nu$. In this case, $r(t) = \Gamma_0 p(t - t_0)$. Alternatively, the SRF may arise from a Green's function linked with a physical system, for example, fluorescence lifetime [12].

The reflected signal $r(t)$ then interacts with the sensor equipped with some instrument response function (IRF) and the measurements are recorded in the form,

$$m(t) = \int r(\tau) \underbrace{\varphi(t,\tau)}_{\text{IRF}} d\tau \tag{2}$$

where φ may be the point spread function of a lens (spatial context) or the temporal response of a transducer, for example, the ultrasound detector in the case of PA imaging. Typically, m is sampled $m_k = m(kT_s), k \in \mathbb{Z}$ where $T_s > 0$ is the sampling rate. Furthermore, whenever h and φ are shift-invariant, that is, $h(t,\tau) = h(t-\tau)$, the measurements simplify to a convolution/filtering equation,

$$m(t) = (p * h * \varphi)(t). \tag{3}$$

Next, we will discuss the probing function, the SRF and the IRF that stem from the PA imaging problem.

B. From PA Wave Equations to Time-of-Flight

We use capitalized symbols $\mathsf{P}, \mathsf{T}, \mathsf{H}$ to denote the spatio-temporal functions with arguments $\vec{r} = (x, y, z)^\top$ (spatial co-ordinates) and t (time), that is, $\mathsf{P}(\vec{r}, t)$, and so on. The PA effect is explained by coupled differential equations based on temperature T and pressure P [14],

$$\begin{cases} \frac{\partial}{\partial t}(\mathsf{T} - \kappa_1 \mathsf{P}) = \kappa_2 \nabla^2 \mathsf{T} + \kappa_3 \mathsf{H} \\ \Box_\nu \mathsf{P} = \kappa_4 \partial_t^2 \mathsf{T} \end{cases}$$

where

- $\nabla^2(\cdot)$ is the Laplace operator, $\Box_\nu = \nabla^2 - \nu^{-2}\partial_t^2$ is the d'Alembert operator and ν is the speed of sound in given medium.
- $\{\kappa_m\}_{m=1}^4$ are some physical constants (for details, we refer to [5]).
- $\mathsf{H}(\vec{r}, t)$ is the heat or thermal energy attributed to the electromagnetc or EM radiation of the optical excitation pulse.
- $\mathsf{P}(\vec{r}, t)$ is the resultant acoustic pressure wave.

In practice, it is justifiable that the thermal conductivity is zero and the P–T coupled differential equations reduce to (cf. pg. 4 in [5]),

$$\Box \mathsf{P} \equiv \left(\nabla^2 - \frac{1}{\nu^2}\partial_t^2\right) \mathsf{P} = -\kappa \partial_t \mathsf{H}. \tag{4}$$

In the case of one-dimensional propagation, $\vec{r} = (0, 0, z)^\top$, the above admits a simple solution based on the integral equation, $\mathsf{P}(z,t) = \frac{\kappa\nu}{2} \int \mathsf{H}\left(r, t - \frac{z-r}{\nu}\right) dr$. Consider an instantaneous source $\mathsf{H}(z,t) = \delta(t)\,\delta(z)$ and a reflective surface at $z = z_0 > 0$. In that case [15],

$$\mathsf{P}(z,t) = \underbrace{\delta\left(t - \tfrac{z}{\nu}\right)}_{\text{(a)}} + \underbrace{\delta\left(t - \tfrac{z+2z_0}{\nu}\right)}_{\text{(b)}}, \tag{5}$$

where (a) arises from the direct excitation of energy which is delayed by the travel time of sound and (b) is the travel time between the source and the reflective surface (cf. Fig. 3(a)). Furthermore, if we consider $\mathsf{H}(z,t) = p(t)\,\delta(z)$ where p is temporal probing function, we obtain a convolution between $\mathsf{P}(z,t)$ and p, ignoring a constant dilation $\propto \nu$. This is consistent with the experiments in layered media (cf. Fig. 4, [16])

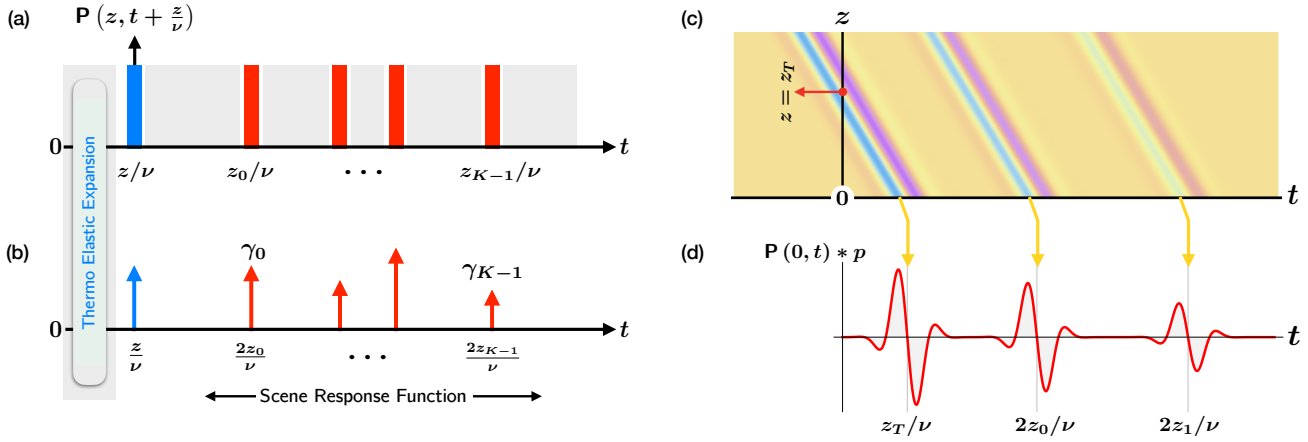

Fig. 3. Photoacoustic waves in layered media. All figures should be understood in sense of negative time. (a) Geometrical setup with K reflecting boundaries or layers. The first reflective surface marked in blue is virtual. Optical excitation causes thermo elastic expansion resulting in sound waves and $t = z/\nu$ is the instant at which sound waves travel to the source. There on, sound waves are reflected from each layer at $t = z_k/\nu$. (b) Corresponding scene respond function. Here, each reflecting boundary results in a round trip travel time of $t_k = 2z_k/\nu$. (c) We plot the propagating wave, $\mathsf{P}(z,t)$ in the case of optical excitation $\mathsf{H}(z,t) = \delta(z - z_T)\, p(t)$, where the probing function $p(t)$ is chosen to be a Gabor pulse. (d) Time-domain waves reflected towards the source at $z = 0$.

as well as the convolution equations in acoustic microscopy (cf. pg. 152, [10]). In general, for the case of K reflecting boundaries at $z = z_k$ with reflection coefficient γ_k, we have,

$$h(t,\tau) \equiv \mathsf{P}(z, t-\tau) = \sum\nolimits_{k=0}^{K-1} \gamma_k \delta\left(t - \tau - \tfrac{z+2z_k}{\nu}\right), \quad (6)$$

which also serves as our SRF for the PA imaging context. In Fig. 3(b) we plot the SRF corresponding to the general case of K reflective surfaces. With $K = 2$ and optical excitation of the form,

$$\mathsf{H}(z,t) = \delta(z - z_0)\, p(t)$$

we plot the pressure wave $\mathsf{P}(z,t)$ in Fig. 3(c) and the corresponding time-domain waveform at $z = 0$ in Fig. 3(d).

Typically, the incoming pressure wave is sensed through an ultrasound transducer with some IRF, φ. Furthermore, by ignoring the constant offset of z_T/ν due to virtual source (or the delayed sound wave), we model the measurements as,

$$m(t) = \left(p * \mathsf{P}\left(0, t + \tfrac{z}{\nu}\right) * \varphi\right)(t) = \sum\nolimits_{k=0}^{K-1} \gamma_k \left(p * \varphi\right)\left(t - 2\tfrac{z_k}{\nu}\right). \quad (7)$$

C. Tomographic Measurements for Geometric Estimation

Blood cells have distinct geometrical features based on their shape, size and morphology. Here, we will focus on the RBCs. As shown in Fig. 4, tomographic measurements of the RBCs leads to a functional relationship between ToF and the orientation of the RBC. In Fig. 4, measurements at $\theta = 0$ are associated with the smallest possible ToF. This corresponds to the horizontal configuration in Fig. I where the experimentally obtained time-domain measurements are relatively concentrated when compared to the vertical configuration, $\theta = \pi/2$. We may therefore write,

$$m_\theta(t) \overset{(7)}{=} \sum\nolimits_{k=0}^{K-1} \gamma_k^{(\theta)} \left(p * \varphi\right)\left(t - t_k^{(\theta)}\right), \quad t_k^{(\theta)} \triangleq 2\frac{z_{k,\theta}}{\nu}. \quad (8)$$

Ideally, for the case of cell imaging, $K = 2$. Since RBCs are bi-concave, $\Delta_\theta = |t_1^{(\theta)} - t_0^{(\theta)}|$ is a proxy of its relative orientation with respect to the source. On the other hand WBCs are spherical and $\Delta_\theta = |t_1^{(\theta)} - t_0^{(\theta)}| \propto 2\rho$ where ρ is the radius. As a result, $\{\theta, \Delta_\theta\}$ may be used to characterize the geometry of cells (in our case) and a layered enclosure, in general. In practice, one acquires measurements of the form,

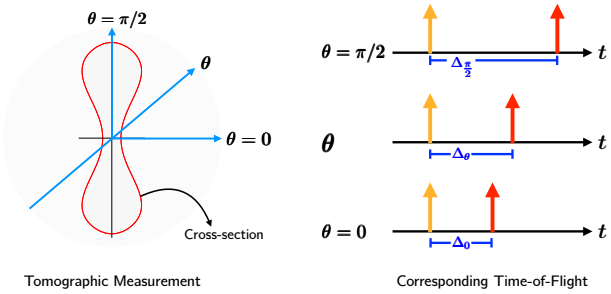

Fig. 4. Tomography of RBCs. At each θ, reflections from the cell walls (layered media) result in a distinct time-of-flight, $\Delta_\theta = |z_1 - z_0|$. Note that Δ_θ encodes the geometric properties of the enclosure which may be RBC, WBC or CMC.

$$m_{\theta_\ell}(nT_s), n = 0, \ldots, N-1, \quad \left\{\theta_\ell = \tfrac{2\pi}{L}\ell\right\}_{\ell=0}^{L} \quad (9)$$

and the inverse problem is to recover $\{\gamma_k^{(\theta)}, t_k^{(\theta)}\}_{k=0}^{K-1}$ from which Δ_θ may be estimated. In this work, we will restrict ourselves to $K = 2$.

III. Inverse Problem: Estimating Time-of-Flight

In order to recover unknowns $\{\gamma_k^{(\theta)}, t_k^{(\theta)}\}_{k=0}^{K-1}$ from (9), we will begin with writing $p * \varphi = \phi$ in (8). Furthermore, we will *approximate* ϕ with trigonometric moments [9], [17], [18], $u_m(\omega_0 t) \triangleq e^{jm\omega_0 t}$,

$$\phi(t) \approx \widetilde{\phi}(t) = \sum\nolimits_{|m| \leqslant M} b_m u_m(\omega_0 t), \quad (10)$$

where b_m's are Fourier series coefficients and $\omega_0 = 2\pi/NT_s$, assuming that $T_0 = NT_s$ is large enough that all the K reflections are observed. This is typically the case in almost all pulse-echo ToF systems [9], [12]. Here, $\omega_0 M \approx \Omega_m$ and M is a function of the transducer bandwidth. By substituting the approximation of ϕ in (8), we obtain,

$$m_\theta(t) = \sum\nolimits_{|m| \leqslant M} b_m \sum\nolimits_{k=0}^{K-1} \gamma_k^{(\theta)} u_m(\omega_0 t - \omega_0 t_k^{(\theta)}),$$

and since u_m is separable, $u_m(f+g) = u_m(f)\, u_m(g)$, we have,

$$m_\theta(t) = \sum\nolimits_{|m| \leqslant M} b_m \widehat{h}_m^{(\theta)} u_m(\omega_0 t)$$

Algorithm 1: Photoacoustic Time-of-Flight Estimation

Data: Measurements $m_\theta(nT_\mathsf{s})$ in (9) with $N \geq 2M+1$ with $M \geq 2$.
Result: Cell Parameters: $\{\gamma_0^{(\theta)}, \gamma_1^{(\theta)}, t_0^{(\theta)}, t_1^{(\theta)}\}$ and $\Delta_\theta = |t_1^{(\theta)} - t_0^{(\theta)}|$.
1) Estimate $\widehat{\mathbf{h}}^{(\boldsymbol{\theta})} = \mathbf{U}^{+}\mathbf{D}_b^{+}\mathbf{m}_{\boldsymbol{\theta}}$ (12) where $^+$ is the matrix psuedo inverse.
2) Given $\widehat{\mathbf{h}}^{(\boldsymbol{\theta})}$, estimate $\{\widetilde{\lambda}_0, \widetilde{\lambda}_1\}$ using (13).
3) With $\{\widetilde{\lambda}_0, \widetilde{\lambda}_1\}$ known, solve for $\mathcal{Q}(x) = 0 \to \{\widetilde{\mu}_0, \widetilde{\mu}_1\}$ and hence, the time-of-flight $\widetilde{t}_k^{(\theta)} = -\angle\widetilde{\mu}_k/\omega_0$.
4) The estimates $\{\widetilde{\gamma}_0^{(\theta)}, \widetilde{\gamma}_1^{(\theta)}\}$ are obtained using least-squares solution,

$$\underset{\{\gamma_0^{(\theta)}, \gamma_1^{(\theta)}\}}{\arg\min} \sum\nolimits_n \left| m(nT) - \gamma_0^{(\theta)}\widetilde{\phi}(nT - \widetilde{t}_0^{(\theta)}) - \gamma_1^{(\theta)}\widetilde{\phi}(nT - \widetilde{t}_1^{(\theta)}) \right|^2$$

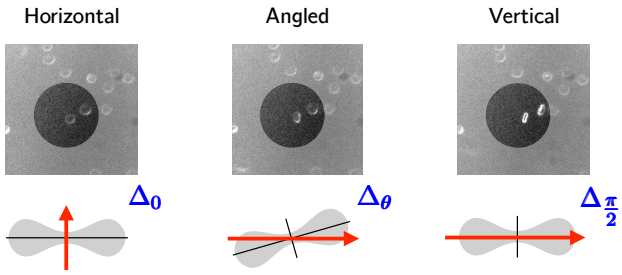

Fig. 5. Optical images of RBCs at various orientations ranging from horizontal to vertical. Optical images are used to register with corresponding PA measurements.

where,

$$\widehat{h}_m^{(\theta)} = \sum\nolimits_{k=0}^{K-1} \gamma_k^{(\theta)} u_m^*\left(\omega_0 t_k^{(\theta)}\right), \quad m = -M, \ldots, M \tag{11}$$

are the Fourier series coefficients of the sparse SRF denoted by $h_\theta(t) = \sum_{k=0}^{K-1}\gamma_k^{(\theta)}\delta(t - t_k^{(\theta)})$. The above, (11), is the standard form of equation that shows up in context of spike deconvolution [17], time-delay estimation [19] and sampling theory [20]. Given sampled measurements in (9), we stack them in vector–matrix form,

$$\mathbf{m}_{\boldsymbol{\theta}} = \mathbf{U}\mathbf{D}_b\widehat{\mathbf{h}}^{(\boldsymbol{\theta})} \tag{12}$$

where,

- $\mathbf{m}_{\boldsymbol{\theta}} \in \mathbb{R}^N$ is a vector of measured data (cf. Fig. I).
- $\mathbf{U} \in \mathbb{C}^{N\times(2M+1)}$ is a DFT matrix with elements $\left[e^{\jmath m\omega_0 nT_\mathsf{s}}\right]_{n,m}$.
- $\mathbf{D}_b \in \mathbb{C}^{(2M+1\times 2M+1)}$ is a diagonal matrix with diagonal elements $b_{m,m} = \widehat{\phi}(m\omega_0)$.
- $\widehat{\mathbf{h}}^{(\boldsymbol{\theta})} \in \mathbb{C}^{2M+1}$ is a vector whose elements are the Fourier transform of the SRF (cf. (11)).

Since (12) is a linear system of equations, we can estimate $\widehat{\mathbf{h}}^{(\boldsymbol{\theta})}$ directly provided that $\{b_m\}_m$ are known. With $\widehat{\mathbf{h}}^{(\boldsymbol{\theta})}$ known, we will use trigonometric interpolation [17], [20], [21] to estimate the unknowns $\{\gamma_0^{(\theta)}, \gamma_1^{(\theta)}, t_0^{(\theta)}, t_1^{(\theta)}\}$. While trigonometric interpolation works for finite K, for the specific case hand, $K = 2$, we outline a closed form solution (assuming noiseless setting). For this purpose, let us define, $\mu_k^m \triangleq u_1^*(\omega_0 t_k^{(\theta)})$ and hence, we have, $\widehat{h}_m^{(\theta)} = \mu_0^m + \mu_1^m$, resulting in,

$$\begin{array}{ll} \widehat{h}_0^{(\theta)} = \gamma_0^{(\theta)} + \gamma_1^{(\theta)} & \widehat{h}_1^{(\theta)} = \gamma_0^{(\theta)}\mu_0 + \gamma_1^{(\theta)}\mu_1 \\ \widehat{h}_2^{(\theta)} = \gamma_0^{(\theta)}\mu_0^2 + \gamma_1^{(\theta)}\mu_1^2 & \widehat{h}_3^{(\theta)} = \gamma_0^{(\theta)}\mu_0^3 + \gamma_1^{(\theta)}\mu_1^3 \end{array}.$$

Let $\mathcal{Q}(x) = (x-\mu_0)(x-\mu_1) = x^2 + \lambda_1 x + \lambda_0$ be some quadratic polynomial. It follows that, $\mathcal{Q}(\mu_k) = 0 = \mu_k^2 + \lambda_1\mu_k + \lambda_0$, $k = 0, 1$. Based on this, we can write,

$$\underbrace{\mathcal{Q}(\mu_0) = \mathcal{Q}(\mu_1)}_{=0} \Leftrightarrow \left\{ \begin{array}{l} \gamma_0^{(\theta)}\mathcal{Q}(\mu_0) + \gamma_1^{(\theta)}\mathcal{Q}(\mu_1) = 0 \\ \gamma_0^{(\theta)}\mu_0\mathcal{Q}(\mu_0) + \gamma_1^{(\theta)}\mu_1\mathcal{Q}(\mu_1) = 0 \end{array} \right.$$

which is equivalent to solving the linear system of equations,

$$\begin{bmatrix} \widehat{h}_0^{(\theta)} & \widehat{h}_1^{(\theta)} \\ \widehat{h}_1^{(\theta)} & \widehat{h}_2^{(\theta)} \end{bmatrix} \begin{bmatrix} \lambda_0 \\ \lambda_1 \end{bmatrix} = -\begin{bmatrix} \widehat{h}_2^{(\theta)} \\ \widehat{h}_3^{(\theta)} \end{bmatrix}. \tag{13}$$

Hence, at a fixed θ and noiseless conditions, four values of $\widehat{h}_m^{(\theta)}$ suffice to compute the four unknowns. This is accomplished by implementing the algorithm outlined in Algorithm 1. Next, we experimentally validate our approach and discuss practical aspects of our implementation.

IV. Photoacoustic ToF Imaging: Experimental Verification

Our proposed approach is validated via experiments using PA imaging setup and the data is acquired using the procedure described in [7].

A. ToF Estimation of RBCs

In the first case, we consider RBCs at four different orientations. For this purpose, PA measurements m_θ are acquired using the experiments in [7]. Conceptually, this is similar to tomography as shown in Fig. 5. As the RBC rotates from horizontal to vertical state, one should expect the ToF to increase (cf. Fig. 4). As highlighted in the literature [7], previously, this was not possible. Here we model ϕ as a Gabor pulse. While this choice is heuristic, in our experience, and as will be shown shortly, this achieves near exact performance (in context of the maximum likelihood estimation or the MLE). As an approximation to the transducer response, the bandpass pulse is chosen such that its maximum response is between 200 to 500 MHz [8], [11]. With ϕ in place, we use a finite Fourier series approximation which specifies $\{b_m\}$ in (10) and hence $\mathbf{D}_b$ [9], [12] with $M = 18$ and $f_0 = \omega_0/2\pi = 25.80$ MHz. To deal with model mismatch and noise in experimental data, we replace steps 1) and 2) in Algorithm 1 with Cadzow's method [22].

In Fig. 6(a), we plot $\{m_{\theta_\ell}(nT_\mathsf{s})\}_{\ell,n}$ (cf. (9)) with $T_\mathsf{s} = 0.125$ ns, $N = 311$ and $\theta = 0$ to $\pi/2$ (approximately) in 108 steps, which we call, time-resolved *pixel*. For each of the four orientations, the PA signal or the time-resolved pixel is plotted in Fig. 6 (a_1) to (a_4). The estimated locations of layers or cell walls, that is $\{\gamma_k^{(\theta)}, t_k^{(\theta)}\}_{k=0,1}$ are also marked. Since this is the case of $K = 2$, it is possible to compare our results with exhaustive search or MLE. Hence we also compute the MLE estimates, $\{\gamma_k^{(\theta)}, t_k^{(\theta)}\}_{k=0,1}$. We use peak signal-to-noise ratio or PSNR denoted by η as our performance metric. The results are summarized as follows:

	θ_1	θ_1	θ_1	θ_1	units
η_{MLE}	32.97	31.05	35.88	35.89	dB
η_{PSR}	32.97	31.05	34.61	35.88	db
Size/ToF	5.780	5.300	3.820	1.960	μm

where η_{PSR} is the PSNR due to PA–ToF super-resolution and η_{MLE} is due to the MLE and we use $\nu = 1570$ m/s. Since we rely on optical microscopy (cf. Fig. 5) for estimating orientation angle θ, the registration between θ and $m_\theta(t)$ is challenging. However, near exact performance in context of MLE suggests that the PA–ToF can recover a proxy of the orientation which can be used to discern features. To exemplify this point, we move to the next case.

B. ToF Estimation of Melanoma Cells

In Fig. 6(b), we plot PA measurements for CMCs. With $K = 4$, we super-resolve measurements and plot $\{\gamma_k^{(\theta)}, t_k^{(\theta)}\}_{k=0,3}$. The reconstruction accuracy is $\eta_{\mathsf{PSR}} = 33.07$ db. We note that $|\gamma_0^{(\theta)}|$ and $|\gamma_2^{(\theta)}|$ correspond to the dominant reflections. Based on this, we compute the ToF which is $\Delta = 10.75$ ns. The corresponding cell size is $\Delta\nu = 16.87$ μm. This is consistent with the results in [11]. Clearly, the estimated cell size is the distinct feature which distinguishes CMCs from RBCs.

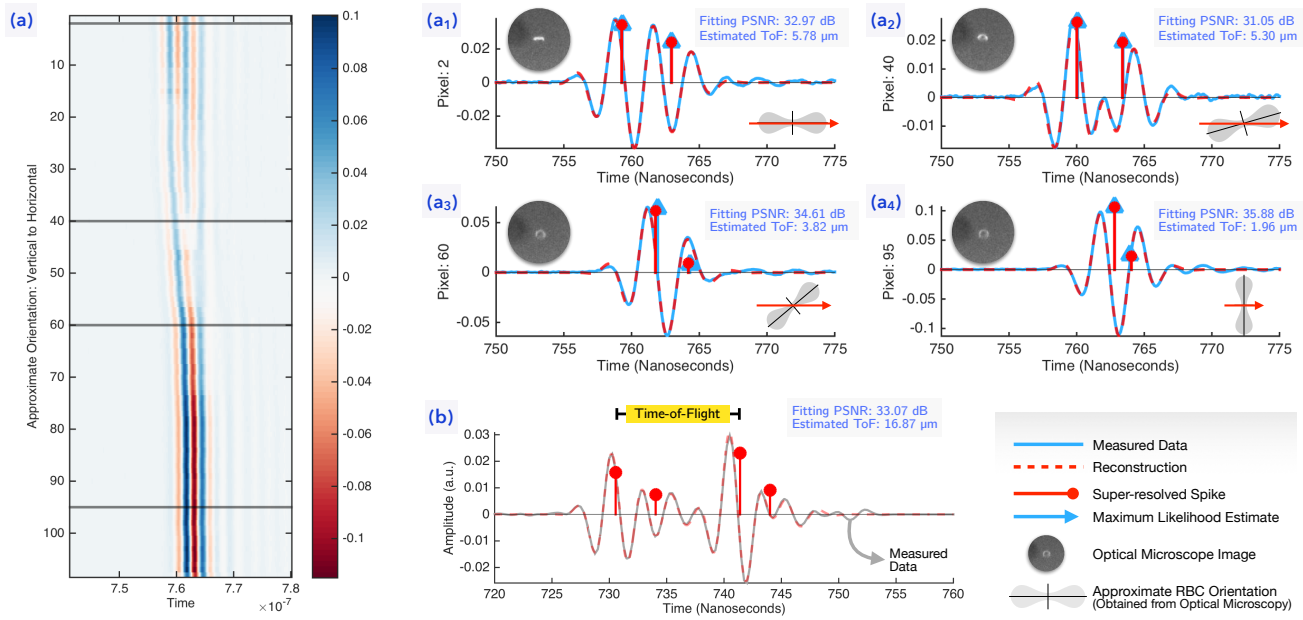

Fig. 6. (a) Photoacoustic measurements $\{m_{\theta_\ell}(nT_s)\}_{\ell,n}$ with $T_s = 0.125$ ns, $N = 311$ and θ_ℓ ranging from vertical to horizontal orientation in 108 steps. (a_1) to (a_4) We plot PA measurements for four orientations. In the inset, we plot the optical image of the single cell RBC together with an approximate orientation angle. The measured data in blue ink (——). Super–resolved SRF specified by $\{|\gamma_k^{(\theta)}|, t_k^{(\theta)}\}_{k=0,1}$ in (6) and (8) is marked in red ink (—●). Based on the estimates $\{|\widetilde{\gamma}_k^{(\theta)}|, \widetilde{t}_k^{(\theta)}\}_{k=0,1}$, the reconstructed data $\widetilde{m}_\theta$ (8) is plotted in red ink (- - -). Reconstruction quality metric, the PSNR and the ToF are also annotated in the inset. Finally, we show the result of maximum likelihood estimation (exhaustive search) with blue spikes (—▶). (b) PA measurements of melanoma cells (CTC). We show the data in gray ink (——). Super–resolved SRF, $\{|\gamma_k^{(\theta)}|, t_k^{(\theta)}\}_{k=0,3}$ is marked in red ink (—●) and the reconstructed data is plotted in red ink (- - -).

V. Conclusion

Starting with a forward model for the photoacoustic phenomenon, we compare the measurements of blood cells to a sum of overlapping echoes. Instead of using the exact physical model, we approximate the measurements with an empirical pulse that confirms with physical characteristics of our measurement device. We represent such pulses with a finite number of trigonometric moments. Based on this approximate representation, we use trigonometric interpolation for time-of-flight super-resolution. Experimentally acquired tomographic measurements validate our model. While this study is in a preliminary stage, it offers a compelling solution to a bottleneck in photoacoustic imaging. Our work raises several questions in the direction of classification of cellular features and this will be addressed in our future studies.

References

[1] L. V. Wang and J. Yao, "A practical guide to photoacoustic tomography in the life sciences," *Nature Methods*, vol. 13, no. 8, pp. 627–638, Jul. 2016.

[2] A. G. Bell, "On the production and reproduction of sound by light," *Biophys J*, vol. s3-20, no. 118, pp. 305–324, Oct. 1880.

[3] M. Xu and L. V. Wang, "Photoacoustic imaging in biomedicine," *Rev. Sci. Instrum.*, vol. 77, no. 4, p. 041101, Apr. 2006.

[4] F. Gao, X. Feng, and Y. Zheng, "Advanced photoacoustic and thermoacoustic sensing and imaging beyond pulsed absorption contrast," *Journal of Optics*, vol. 18, no. 7, p. 074006, May 2016.

[5] L. V. Wang, *Photoacoustic Imaging and Spectroscopy*, ser. Optical Science and Engineering. CRC Press, Mar. 2009.

[6] G. J. Diebold, M. I. Khan, and S. M. Park, "Photoacoustic "signatures" of particulate matter: Optical production of acoustic monopole radiation," *Science*, vol. 250, no. 4977, pp. 101–104, Oct. 1990.

[7] E. M. Strohm and M. C. Kolios, "Classification of blood cells and tumor cells using label-free ultrasound and photoacoustics," *Cytometry Part A*, vol. 87, no. 8, pp. 741–749, Jun. 2015.

[8] E. M. Strohm, E. S. Berndl, and M. C. Kolios, "Probing red blood cell morphology using high-frequency photoacoustics," *Biophysical Journal*, vol. 105, no. 1, pp. 59–67, Jul. 2013.

[9] A. Bhandari and R. Raskar, "Signal processing for time-of-flight imaging sensors: An introduction to inverse problems in computational 3-D imaging," *IEEE Signal Processing Magazine*, vol. 33, no. 5, pp. 45–58, Sep. 2016.

[10] G. A. D. Briggs and O. Kolosov, "Experimental elastic microanalysis," in *Acoustic Microscopy*. Oxford University Press (OUP), Sep. 2009, pp. 123–159.

[11] E. M. Strohm, M. J. Moore, and M. C. Kolios, "Single cell photoacoustic microscopy: A review," *IEEE J. Sel. Topics Quantum Electron.*, vol. 22, no. 3, pp. 137–151, May 2016.

[12] A. Bhandari, C. Barsi, and R. Raskar, "Blind and reference-free fluorescence lifetime estimation via consumer time-of-flight sensors," *Optica*, vol. 2, no. 11, pp. 965–973, Nov. 2015.

[13] A. Bhandari, A. Kadambi, R. Whyte, C. Barsi, M. Feigin, A. Dorrington, and R. Raskar, "Resolving multipath interference in time-of-flight imaging via modulation frequency diversity and sparse regularization," *Optics Letters*, vol. 39, no. 6, pp. 1705–1708, Mar. 2014.

[14] P. M. Morse and K. U. Ingard, *Theoretical acoustics*. Princeton university press, 1968.

[15] G. J. Diebold, "Photoacoustic waves at reflecting interfaces," *Review of Scientific Instruments*, vol. 74, no. 1, pp. 801–804, Jan. 2003.

[16] T. J. Allen and P. C. Beard, "High power visible light emitting diodes as pulsed excitation sources for biomedical photoacoustics," *Biomedical Optics Express*, vol. 7, no. 4, p. 1260, Mar. 2016.

[17] T. P. Speed and L. Li, "Parametric deconvolution of positive spike trains," *The Annals of Statistics*, vol. 28, no. 5, pp. 1279–1301, oct 2000.

[18] J. Urigüen, T. Blu, and P.-L. Dragotti, "FRI sampling with arbitrary kernels," *IEEE Trans. Sig. Proc.*, vol. 61, no. 21, pp. 5310–5323, Nov. 2013.

[19] J. Li and R. Wu, "An efficient algorithm for time delay estimation," *IEEE Trans. Sig. Proc.*, vol. 46, no. 8, pp. 2231–2235, Aug. 1998.

[20] M. Vetterli, P. Marziliano, and T. Blu, "Sampling signals with finite rate of innovation," *IEEE Trans. Sig. Proc.*, vol. 50, no. 6, pp. 1417–1428, 2002.

[21] R. L. Stoica, P. and Moses, *Introduction to spectral analysis*. Prentice hall Upper Saddle River, 1997, vol. 1.

[22] J. Cadzow, "Signal enhancement-a composite property mapping algorithm," *IEEE Trans. Acoust., Speech, Signal Process.*, vol. 36, no. 1, pp. 49–62, Jan. 1988.